Low temperature spintronics: Probing charge and spin states with two-dimensional electron gas

by

Wing Wa Yu

B.Sc., University of Iceland, 2006

A THESIS SUBMITTED IN PARTIAL FULFILLMENT OF THE REQUIREMENTS FOR THE DEGREE OF

MASTER OF SCIENCE

in

The Faculty of Graduate Studies

(Physics)

THE UNIVERSITY OF BRITISH COLUMBIA

(Vancouver)

August 2009

Abstract

This thesis is based on two low temperature experiments in spintronics – physics and engineering of electronic spins. The measurements were performed on a GaAs/AlGaAs two-dimensional electron gas with geometries defined by tunable surface gates.

The first experiment is about detection of electrons in a quantum dot. A quantum point contact (QPC) and a quantum wire (QW) is coupled to a single-lead few-electron quantum dot. By measuring the conductance of the QPC and the QW, one can gain information on the average number of electrons in the dot as well as energy-level structure of the dot.

The second experiment investigates anisotropy of spin-orbit interaction in GaAs/AlGaAs heterostructure by measuring spin polarization in a narrow channel. Polarized electrons are injected into the channel through a spin-selective injector QPC and diffuse towards the end of the channel. This diffusion generates a pure spin current and the spin polarization $25\mu m$ away is measured by a detector QPC. A periodic spin-orbit field induced by motion of the electrons in the channel causes the spins to resonate with external magnetic field. Spin-orbit anisotropy is demonstrated by the different resonance strength observed in channels aligned along two different crystal axes.

Table of Contents

Appendices

List of Figures

Acknowledgements

My most grateful thanks go to my thesis advisor, Joshua Folk. I came to UBC as a graduate student having only done a few experiments during my undergraduate years in physics. Since then, Josh has broadened vastly my understanding in the field of experimental physics and helped me to become a stronger physicist. When I have a question, he is always happy to answer it. When I encounter a technical difficulty, he is always ready to give me a hand. It is due to his guidance and aid that I am now at a point where I can see the successful finish of this thesis and my first graduate degree.

During their post-doctoral stay in Josh's lab, Sergey Frolov and Ananth Venkatesan made valuable contributions to my Masters work with their advice in conducting low-temperature experiments and help in fabricating nano-scale electronic devices. They also made the lab more fun with their good sense of humor. I had a great time working with them.

I would also like to thank my friends. My lab partners Yuan, Chung-Yo, Hadi, Mark and George are great to interact with, whether in the case of discussions about any kind of physics or just casual chat about random things. I thank all my friends and fellow physics students I have met in Vancouver for giving me many new life experiences and making my time here very enjoyable.

Last but not least, I thank my parents and my little brother for all the supports they have given me throughout my life. My parents showed me and my brother the values of pursuing a higher education. Their unselfishness and diligence encouraged me to work harder on my study so that I can become a well-educated person someday. Without them I would not be what I am today. My brother kept me company in many endeavors and the times we spent together are always very cheerful.

Chapter 1

Introduction

This thesis explores two important phenomena found in semiconductor-based spintronic devices: charge sensing with a quantum point contact (QPC) and spin relaxation due to spin-orbit interaction. Spintronics – the study of physical mechanisms related to spins, is essential to achieving better control on them. With deeper understanding on how to manipulate spins, we can build more sophisticated electronic devices. Examples of discoveries that have led to practical spintronic devices are the giant magnetoresistance (GMR) [1–3] and tunnel magnetoresistance (TMR) [4, 5]. These devices made huge impact on computer technology by enabling denser storage of information in hard drives and faster reading of data in random access memories. Continuous research into application possibilities of any spintronic effects is therefore beneficial to realizing more advanced electronics.

All the experiments described in this thesis are performed at a low temperature of a few hundreds to a few tens of Kelvin. At these temperatures, thermal broadening of the Fermi surface is small enough so that it is possible to distinguish between the two electronic spin states. In addition, a charge sensing QPC is only sensitive in the tunneling regime which can only be reached if the thermal energy is smaller than that of the tunnel barrier. Details about QPC are given in chapter 2.

After this introduction, the rest of the thesis is divided into five chapters. Chapter 2 gives an introduction to the semiconductor heterostructure which our spintronic devices are based on, and discusses how devices are implemented. The end of the chapter presents a basic picture on two fundamental spintronics building blocks: QPC and quantum dot. Chapter 3 describes the experiment setup for low temperature measurements. Results of the experiment on detection of electrons in a few-electron quantum dot are shown in chapter 4. Lastly, chapter 5 summarizes the measurements to determine spin-orbit anisotropy. Appendix A lists the fabrication procedures for the devices used in the experiments.

Chapter 2

Two-dimensional electron gas devices

2.1 Semiconductor heterostructure

The spintronic devices described in this thesis are built on a two-dimensional electron gas (2DEG) formed at the interface of a GaAs/$Al_{0.3}Ga_{0.7}As$ semiconductor heterostructure. Compared to other 2D electronic system, this 2DEG offers a larger Fermi wavelength that is comparable to the smallest device size achievable and a much higher mobility. These advantages facilitate the studies of quantum transports in nanostructures. The heterostructure used in the experiments is named D041008B and was grown by Werner Wegscheider in University of Regensburg using molecular beam epitaxy (MBE).

The different semiconductor layers of the GaAs/AlGaAs heterostrucuture are shown in Fig. 2.1. A 75nm layer of AlGaAs is grown epitaxially on a GaAs substrate followed by a 15nm layer of Si n-doped AlGaAs and another 14nm of undoped AlGaAs. A 5nm GaAs cap is then placed on top to prevent oxidation of the surface. Due to the electric field from the positively charged donors in AlGaAs and the bandgap difference of about $0.3eV$ between GaAs and AlGaAs, a triangular potential well is formed at the interface. The potential confinement in the direction perpendicular to the interface creates two-dimensional electronic subbands. At low temperature, only the lowest subband falls below the Fermi energy and becomes populated. As a result, electrons are only allowed to move in a two-dimensional plane, leading to a 2DEG lying 110nm below the surface.

For D041008B, the measured mobility μ is about $4.44 \times 10^6 cm^2/Vs$ [6] which is two orders of magnitude higher than that of 2DEG in Si inversion layer [7]. With an electron density of $n_s = 1.11 \times 10^{11} cm^{-2}$ at 1.5K, the mean free path can be as long as $20\mu m$ [8]. This high mobility stems from the almost identical lattice structure between GaAs and AlGaAs and the large distance between the dopant layer and the interface which helps to reduce scattering from the interface defects and the charged donors.

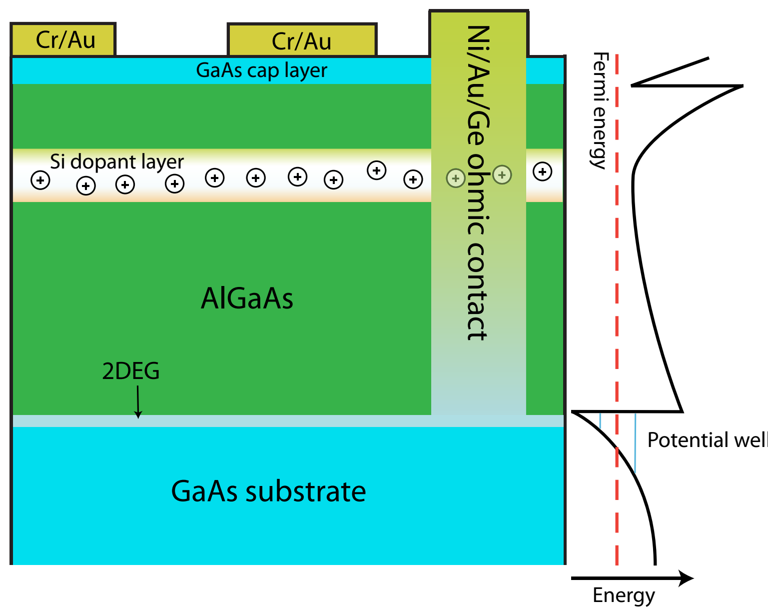

Figure 2.1: Schematic cross-sectional view of GaAs/AlGaAs heterostructure and its band diagram. The heterostructure is constructed by growing doped AlGaAs on a GaAs substrate and then capped with a thin layer of GaAs. The AlGaAs is doped with n-type Si donors at a distance of 75nm from the GaAs/AlGaAs interface where a triangular potential well is formed (shown on the right side). At low temperature, electrons occupy the lowest energy level of the well and the 2DEG is formed. Annealed Ni/Au/Ge ohmic contacts provide electrical connections to the 2DEG and Cr/Au gates control its density capacitively.

2.2 Ohmic contacts and electrostatic gates

To make direct electrical connection to the 2DEG, ohmic contacts made of metal composite of Ni, Ge and Au are deposited on the surface of the heterostructure lithographically. The contacts are then thermally annealed so that the metals diffuse down to the 2DEG and make contact with it. By applying a voltage bias on the ohmics, Fermi energy of the 2DEG can be changed and electrons can be directed from one place to another. Typical resistance of ohmic contacts is in the order of kΩ.

To control density of electrons in the 2DEG, metallic gates of Au and Cr are lithographically patterned on top of the heterostructure. By applying more negative voltage on the gates compared to the 2DEG, regions of the 2DEG directly underneath the gates can be depleted. Electron potential with various shapes and sizes can thus be defined by biasing multiple gates that were deposited in a carefully designed pattern. Details on fabrication of ohmic and gate contacts can be found in Appendix A.

2.3 Quantum point contact

A quantum point contact is the simplest device that manifests quantum mechanical properties of nanostructures. A QPC is a short and narrow constriction formed on a 2DEG with a width comparable to the Fermi wavelength (about 75nm for D041008B). Experimentally, it is implemented by a split gate placed between two ohmic contacts that serve as the source and drain (Fig. 2.2a). When the constriction is narrowed by applying a negative voltage on the gate (V_{gate}), the number of 1D transport modes through the QPC decreases in whole integers. Since each mode contributes $2e^2/h$ to the conductance of the QPC, the measured conductance (G) drops in steps of $2e^2/h \approx (12.9k\Omega)^{-1}$ with a more negative gate voltage (Fig. 2.2b). In high magnetic field, each mode is no longer spin degenerate and the conductance becomes quantized in units of e^2/h [9]. More in-depth discussions on transport through narrow conductors can be found in [7] and [10].

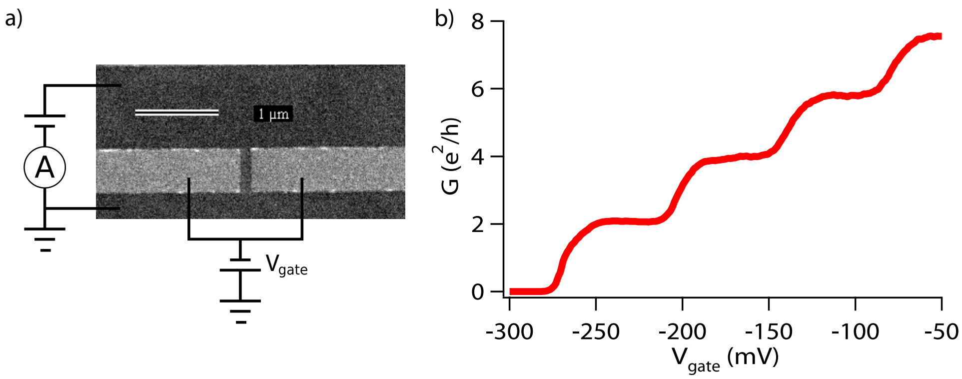

Figure 2.2: a) Scanning electron micrograph (SEM) of a QPC and circuit setup for conductance measurement. The dark area shows the heterostructure surface and bright area is the QPC split gate structure fabricated with electron beam patterning and surface deposition of Cr/Au. b) Conductance G across a QPC drops in steps of $2e^2/h$ as a negative voltage is applied to the QPC gate. The conductance has been corrected due to background resistance of the 2DEG. Edge of the steps is rounded due to thermal averaging.

2.4 Quantum dot and Coulomb blockade

Another important building block of spintronic devices is quantum dot. A quantum dot is a small confined area of electrons in which the energy levels are quantized. In our experiments, a quantum dot is defined by multiple surface gates that electrostatically deplete the 2DEG regions surrounding the dot. Typically, a quantum dot is coupled to a source and drain reservoir via QPCs and its size is controlled by another gate electrode V_g, also called plunger gate (Fig. 2.3a). If both QPC junctions are tuned to a conductance smaller than $2e^2/h$, electrons move into and out of the dot via tunneling and the number of electrons N inside the dot in equilibrium remains an integer. To add or remove an electron charge (e) from the dot, a charging energy of $E_C = e^2/C$ is required, where C is the capacitance of the dot.

When the thermal energy $k_B T$ is much smaller than the charging energy and the level spacing Δ of the dot, transport through the dot can only take place when a charge tunnel onto and off the dot via a single energy level (Fig. 2.4a). If none of the dot levels lies between the Fermi energies of the source and drain, tunneling through the dot is not energetically allowed and no current passes through (Fig. 2.4b). This blocking of current passage is called Coulomb blockade. Through the capacitive coupling of the gate V_g (Fig. 2.3b), chemical potential of the dot can be shifted in a continuous manner. Consequently, as the gate voltage is scanned at a fixed source-drain voltage, conductance peaks spaced at a regular interval can be observed (Fig. 2.4c). These periodic peaks are the Coulomb oscillations and they correspond to the opening of a conductive path through the dot whenever an energy level is lined up to the source and drain chemical potential.

For a $100nm$ by $100nm$ dot, the charging energy is about $4meV$ and the level spacing is around $30\mu eV$ or $350mK$ which is easily achieved in a dilution refrigerator (discussed in Chapter 3). An excellent review on quantum dots can be found in [11].

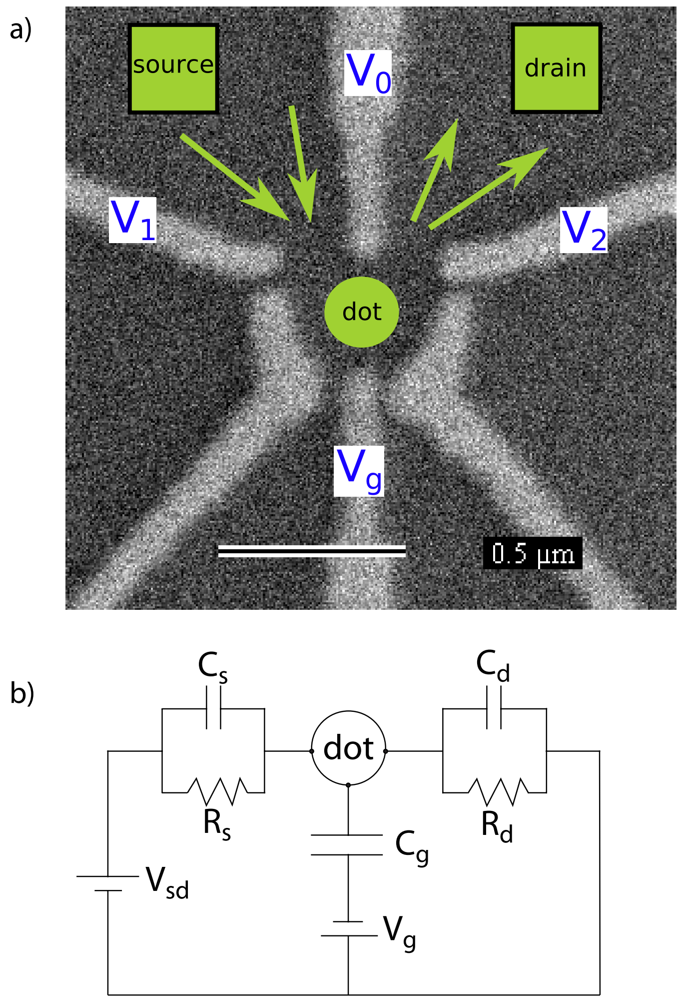

Figure 2.3: a) SEM of a quantum dot defined by surface gates (white color) on a GaAs substrate (dark color). The dot (orange circle) is connected to a source and drain contact (orange square pads) that provide and remove electrons from the dot. Movement of electrons through the source and drain QPC (V_0-V_1 and V_0-V_2 respectively) are shown in orange arrows. Chemical potential of the dot is controlled by the gate V_g. b) Schematic circuit diagram of the quantum dot. The source and drain are capacitively and resistively connected to the dot, while the gate is only capacitively coupled.

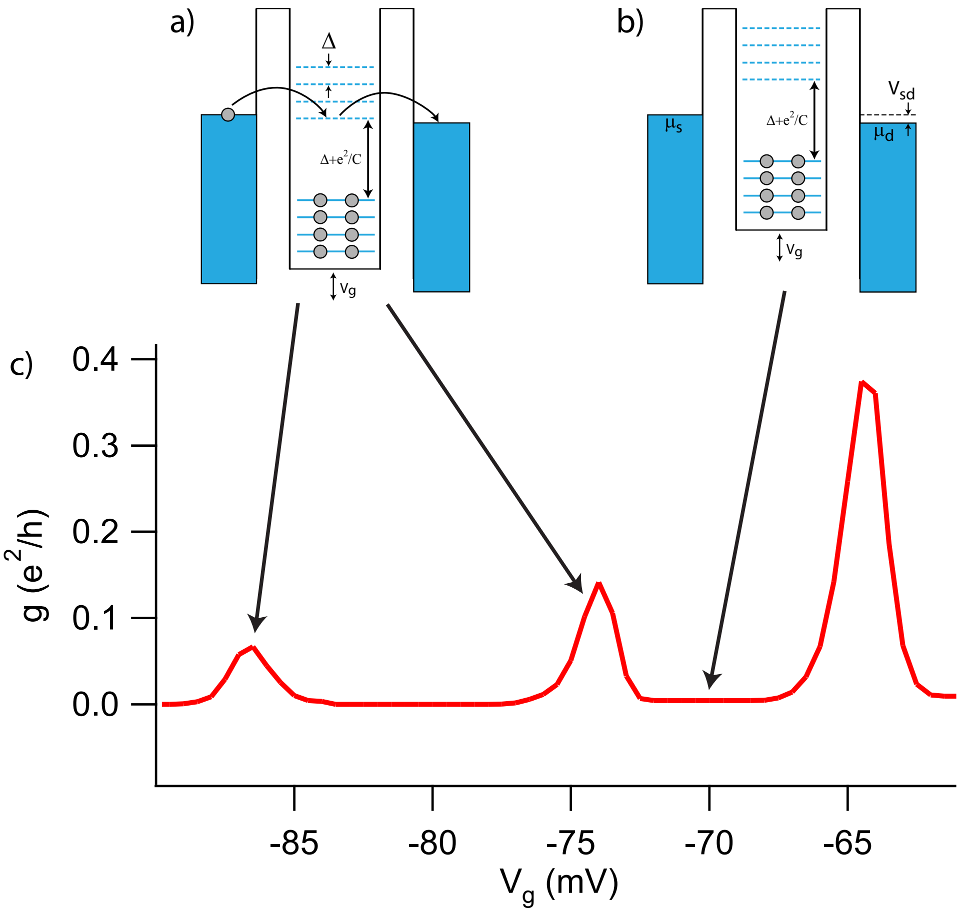

Figure 2.4: a), b) Energy diagram of a quantum dot in the Coulomb blockade regime. Energy difference between levels of the dot is Δ, except the last filled and the next unoccupied level is separated by an additional charging energy of e^2/C. The chemical potential of the dot can be shifted by changing the gate voltage V_g. The source and drain reservoir are continuously filled up to the chemical potential of μ_s and μ_d, respectively. a) When the next unoccupied level is aligned to between μ_s and μ_d, an electron is free to tunnel into and out of the dot, leading to a jump in conductance of the dot (g). b) Current through the dot is blocked as the unoccupied state is shifted up by the gate voltage V_g. c) Coulomb oscillations. Periodic conductance peaks are observed as V_g is swept and new unoccupied state is lined up to the source-drain chemical potentials.

Chapter 3

Low temperature measurement techniques

3.1 Measurement setup

Both experiments in this thesis were carried out at low temperature using a dilution refrigerator. Principle of operation of a dilution refrigerator similar to the one used for this thesis and a guide to the cooling procedures can be found in [12]. The temperature used in the measurements spans from 30mK to 1K. To avoid heating of the sample at such low temperature, bias applied on ohmics and gates are generally kept under $50\mu V$ and $1V$, respectively. Due to the weak signal from the sample, measurements are done using lock-in technique with low frequency AC bias.

A large portion of the experiments in this thesis involve measuring the conductance through QPCs. For this, a two-wire voltage bias circuit is used (Fig. 3.1). The lock-in sourced AC bias and a small DC voltage in the μV range (for non-equilibrium transport measurements) is applied to the QPC source ohmic. This is done through an AC+DC box which divides each component to the suitable magnitude and combines them together. The resulting current through the QPC is amplified by a current preamplifier at the drain and then measured by the lock-in at the AC frequency. A computer running an Igor Pro software controls the QPC gate voltage via a digital-to-analog converter and calculates the conductance based on signals from the lock-in.

There are two other things worth mentioning about the setup. First, the total in-line resistance of each sample wiring in the cryostat is increased to $1k\Omega$ by adding a 600Ω resistor. This is to prevent static discharges from reaching the sample which may cause it to blow up. Second, the ground connections have been broken at several places in the circuit and all instruments have been grounded to a common point. This prevents formation of possible ground loops which can induce extra noise into the signal.

a)

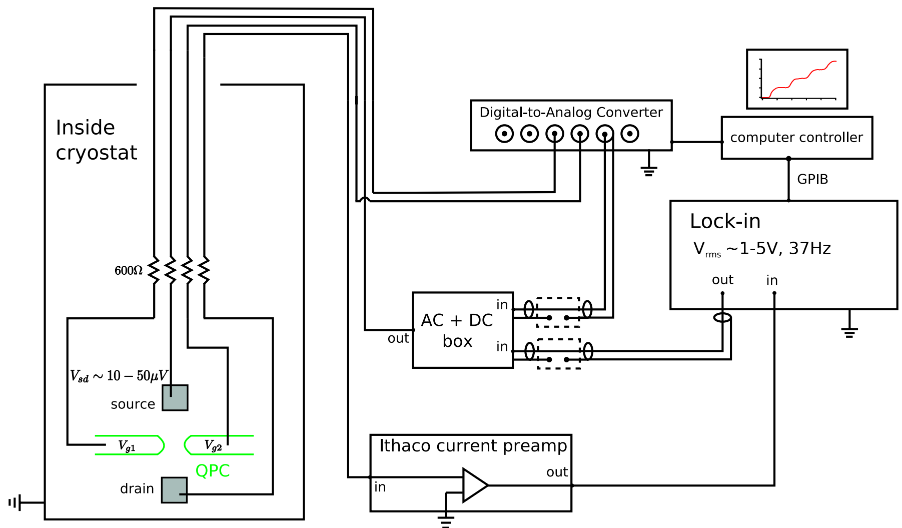

b)

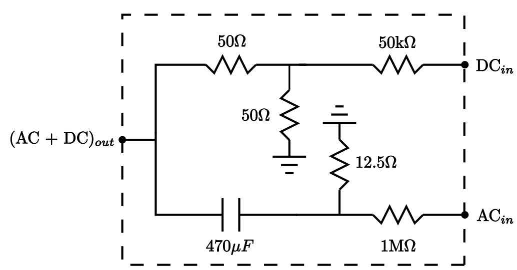

Figure 3.1: a) Circuit setup for QPC conductance measurement. A lock-in sourced AC voltage and a computer controlled DC bias are divided down and combined by an AC+DC box, then applied to the source ohmic. An Ithaco current preamplifier is connected to the drain and outputs the current signal to the lock-in which measures at 37Hz. Gate voltages of the QPC are computer controlled via a digital-to-analog converter. To prevent ground loops, the grounds at the two inputs of the adder box are broken and all equipment grounds are connected together. b) Circuit diagram of the AC+DC box. The box divides an AC and DC bias by a factor of 10^5 and 10^3, respectively, and adds them together.

Chapter 4

Detecting charges in a few-electron quantum dot with QPC via capacitive and resistive coupling

4.1 Introduction

The ability of a QPC to detect change in the number of charges in a nearby quantum dot (QD) was first demonstrated by Field, et al [13]. By tuning the QPC to a conductance below one transport channel ($G < 2e^2/h$), it becomes very sensitive to the local electrostatic landscape. If a charge moved into or out of the QD, the potential of the dot changes and the conductance of the QPC shifts abruptly. This technique becomes extremely useful at characterizing a dot where direct transport through it can not be measured, like in a single-lead dot. Since the first measurement, QPC charge sensing has been thoroughly developed and used extensively to probe charge and spin states in single dots [14, 15] and double dots [16–18]. There are two ways to couple the QPC electrometer to a QD: capacitively and resistively. In the latter case, the charge sensor usually takes the form of a quantum wire (QW) [19–21] and the charge sensing signal is accompanied by Fano interference effect between the discrete states of the QD and the continuous spectrum of the QW.

In this chapter, we describe measurements to determine the charge number in a few-electron dot, using both capacitively coupled QPC and resistively coupled QW charge detectors. Charge detection using the QPC reveals a dot that can confine from a few to zero electrons. The charge sensing signal and the Fano resonance observed in the QW will be presented and discussed.

4.2 Device and measurements

The device (Fig. 4.1) consists of a 120nm by 120nm few-electron dot, a QPC and a QW fabricated on the 2DEG mentioned in Chapter 2. Measurements are performed at 25mK using lock-in techniques. The QD is defined by a triangular gate V_g and a split-gate V_t. V_g tunes the dot potential and V_t controls the tunnel coupling strength Γ_t of the dot to the QW which is defined by V_t and V_w. A charge sensing QPC (V_c and V_g) is placed right outside the dot, and becomes capacitively coupled to the dot when V_g is fully depleted. To prevent pinching off the detector QPC while operating the QD with V_g, a compensating gate voltage is placed on V_c to keep the QPC conductance at the same level.

Instead of looking for jumps in QPC conductance to detect charges in the dot, we used a setup that measures the derivative of the conductance $\frac{dG}{dV_g}$ directly. The AC source bias of the wire oscillates the Fermi level of the quantum dot and adds an effective AC component with the same frequency to the QD gate: $V_g = V_{gDC} + V_{gAC}$. When a DC bias V_{DC} is applied across the QPC, an AC current oscillating at the gate frequency can be detected at the QPC drain. If V_{gAC} is small compared to V_{gDC}, the current is proportional to $\frac{dG}{dV_g}$. We define the ratio of the current and the wire AC bias as the charge sensing signal G_g.

4.3 Results and discussions

The effect of changing the number of electrons N in the dot by tuning V_g on G_g is shown in Fig. 4.2. A peak in G_g indicates an abrupt change in the QPC conductance and therefore highlights a jump in the dot potential. The regularity in peak spacing reflects the energy quantization of the QD

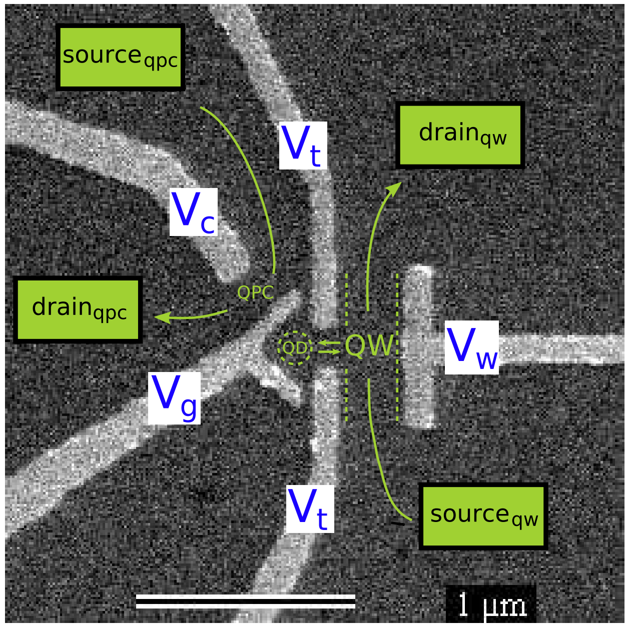

Figure 4.1: SEM of the device used for charge detection experiment. A 120nm by 120nm few-electron dot, defined by V_g and V_t, is coupled to a quantum wire (V_w and V_t) via a tunnel barrier controlled by V_t. To detect the number of charges in the dot, a QPC charge sensor V_c has been capacitively coupled to the dot.

and suggests that the jumps in G_g are result of charge transport through a dot energy level. The absence of regularly spaced peaks at $V_g < -77mV$ indicates that the dot has been emptied at that gate region. Consequently, the region between the first and second peak has one electron in the dot, two electrons between the second and third peak, and so on. The ability of the simple triangular gate structure to tune N down to 0 shows that it works well as a plunger gate.

Fig. 4.3 shows the charge sensing signal G_g and QW conductance G_w as the QD to QW coupling strength V_t and dot potential V_g are varied. The effect of V_t on the wire conductance, which is measured simultaneously as G_g, was canceled by biasing V_w at the same time. With stronger Γ_t (more positive V_t), peaks in G_g become broader which is readily explained

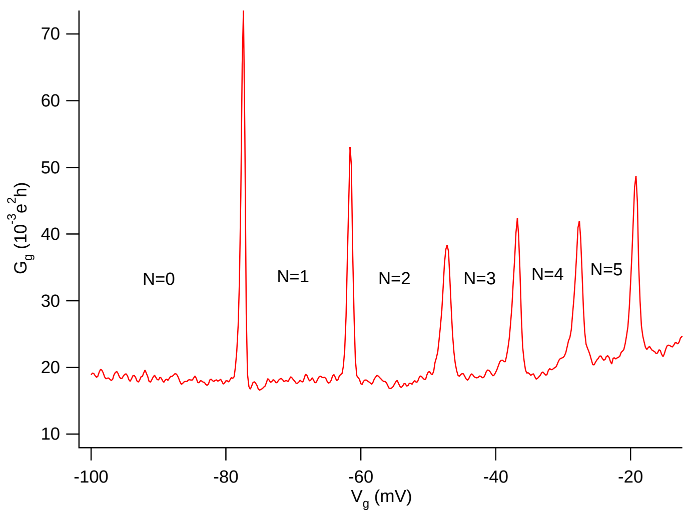

Figure 4.2: G_g is proportional to the derivative of the QPC conductance with respect to V_g. A peak in G_g represents an abrupt change in the QD potential which is a result of charges moving into and out of the QD. In the region between two adjacent peaks, the average number of electrons inside the dot (N) is fixed.

by the broadening of the dot levels due to increased tunneling rate through the lead. At the strong coupling region, $-20mV > V_t > -60mV$, peaks are also broadened as the size of the dot is shrunk with more negative V_g. This is because when the coupling barrier is short, the dot is pushed closer towards the QW as it becomes smaller and this induces more broadening. Spacing between peaks gets larger at lower V_g and V_t (to a lesser extend) as a consequence of larger charging energy E_c with smaller dot size. With a charging energy of $\sim 3meV$ and a peak spacing of $8mV$, the conversion factor α that relates V_g to the chemical potential (μ) of the QD is estimated to be $\alpha = \frac{\Delta\mu}{\Delta V_g} \sim 380\mu eV/mV$.

The wire conductance far from resonance has been adjusted to the first conductance plateau. As seen in Fig. 4.3b), G_w shows dips that share very similar features with the peaks in G_g. Both resonances appear at the same locations, and their width and spacing react to V_g and V_t in the same way.

This shows that the resonance in G_w is originated from the QD. The QW has, therefore, the same ability as the QPC to detect Coulomb oscillations in the dot. The dip structures observed are result of Fano antiresonance which comes from the destructive interference between two conductance paths: a resonant path which goes through the dot and a nonresonant path that only goes through the wire. The asymmetry and lineshape of these resonances can be characterized by the Fano formula [22]:

$$G = A\frac{(\tilde{\epsilon}+q)^2}{\tilde{\epsilon}^2+1} + G_{bg} \tag{4.1}$$

where G_{bg} is the non-vanishing conductance at the resonance minimum [23] and q is the asymmetry parameter. Amplitude of the Fano resonance is represented by A, and the normalized energy

$$\tilde{\epsilon} = \frac{\epsilon - \epsilon_0}{\Gamma/2} = \frac{\alpha(V_g - V_0)}{\Gamma/2} \tag{4.2}$$

depends on the position $\epsilon_0 \equiv \alpha V_0$ and the width Γ of the resonance.

The Fano dips at the four different V_t indicated in Fig. 4.3b are shown in Fig. 4.4a. The most prominent difference between the Fano structures is the dramatic change in resonance asymmetry with coupling strength; a dip with sharp left edge evolves into a symmetric one and then becomes a dip with sharp right edge. Both amplitude and linewidth, on the other hand, become smaller with decreasing Γ_t. The good fit of the resonances to the Fano formula (Fig. 4.4a) suggests that they are indeed effect of destructive interference. The fitting parameters are plotted against coupling strength in Fig. 4.4b, c and d. The change in asymmetry of the resonances is reflected in the change of sign in the asymmetry parameter q. A negative (positive) value represents a sharp left (right) edge dip, while a symmetric dip has $q \sim 0$. This change of sign is likely caused by a slight change in the wire potential induced by V_t, and it can be explained by the finite spatial width of the coupling contact [21]. The decrease in amplitude with weaker coupling is the result of reduced transmission amplitude for the resonant conductance path. In the limit of $\Gamma_t \rightarrow 0$, Fano resonance will eventually disappear as the QD is no longer coupled to the QW, which starts to happen at $V_t \sim -150mV$.

To summarize, we have examined the resonance caused by charge transport through a few-electron dot that appears on the conductance of a charge sensing QPC and a laterally coupled QW. Although caused by different effects, both resonances react in the same way to the number of electrons in the dot and the lead coupling of the dot. This observation suggests that the mechanisms behind both resonances can be used to count electrons and probe charge states in quantum dots.

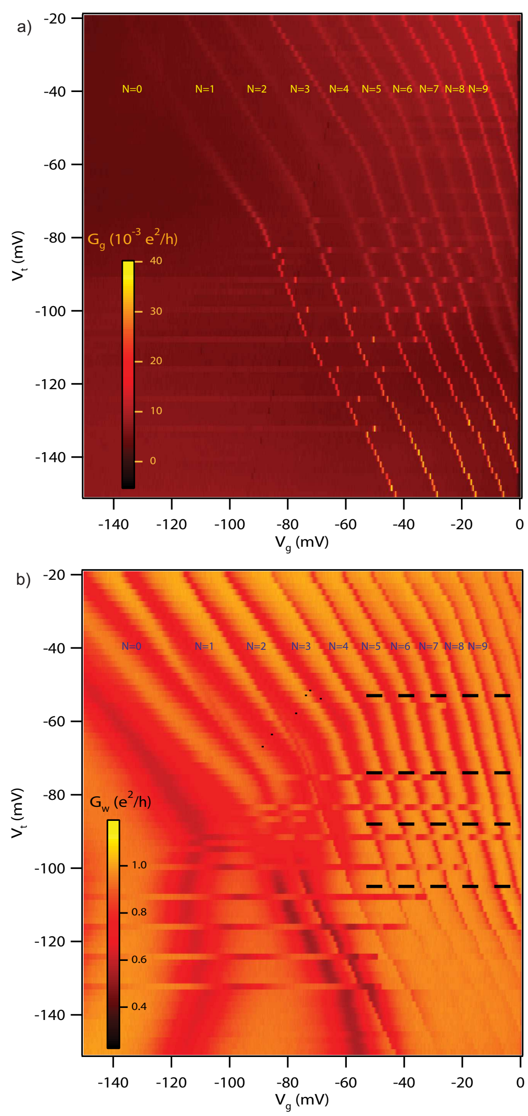

Figure 4.3: Resonance in the charge sensing signal G_g (a) and QW conductance G_w (b) as the dot size and lead coupling Γ_t is varied. More negative V_g and V_t leads to smaller dot size and weaker Γ_t, respectively. a) Resonance peaks become broader with stronger Γ_t. At the open contact regime $(-20mV > V_t > -60mV)$, a smaller dot size means the QD is closer to the contact reservoir which leads to broader peaks. b) Fano antiresonance in the QW conductance. Width (amplitude) of the resonance shows same (opposite) behavior as that of peaks in G_g. Conductance traces along the black dashed lines are shown in Fig. 4.4a.

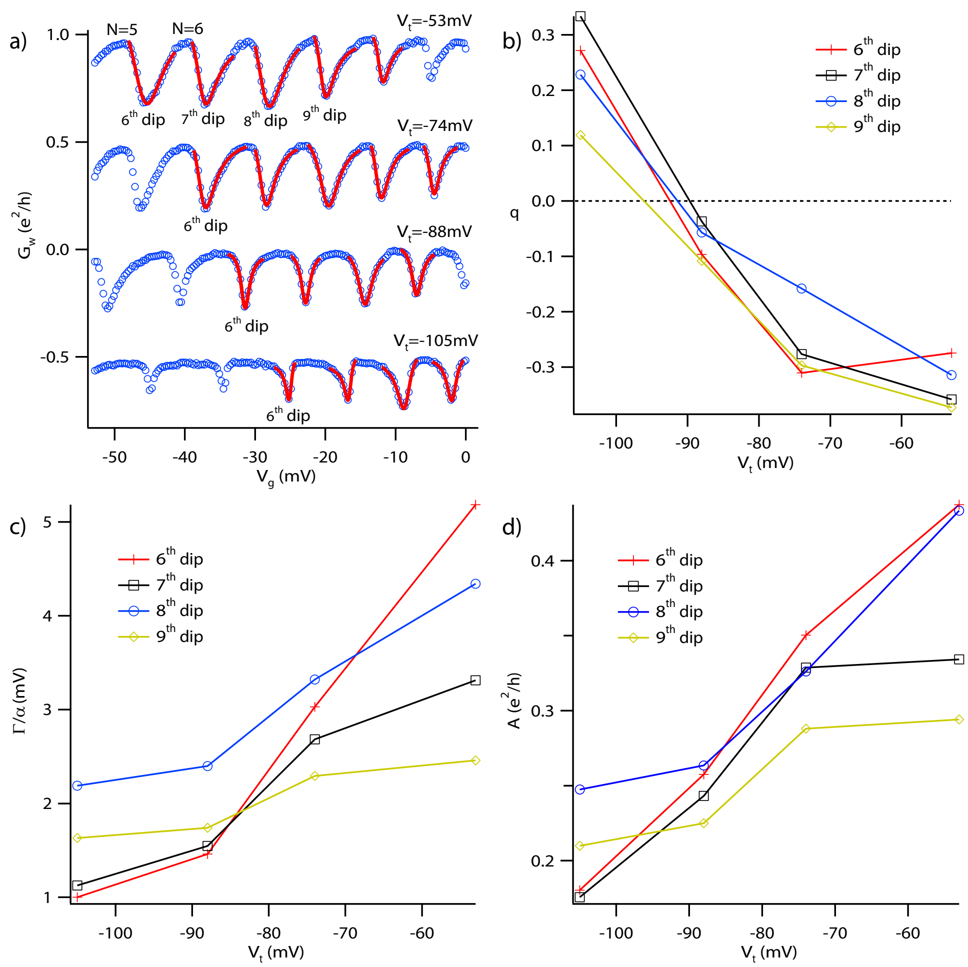

Figure 4.4: a) Fano antiresonance in the QW conductance at the four V_t settings indicated in Fig. 4.3b. Starting from the second trace from the top, the conductance traces are shifted in steps of $0.5e^2/h$ for clarity. The most distinct feature in the resonances is the change in their asymmetry with V_t. This difference is reflected in a change of sign in the asymmetry parameter q of the Fano formula (b). Amplitude A and width Γ from best-fitting of the resonances in a) are shown in c) and d), respectively.

Chapter 5

Anisotropy in spin-orbit interaction measured by ballistic spin resonance

5.1 Introduction

One promising mechanism that could allow coherent manipulation on electron spin is the spin-orbit (SO) interaction. Recent studies have been shown that it has the potential to realize spintronic devices like spin transistor [10], spin interference device [24] and spin filters [25, 26]. In the presence of an electric field, a moving electron experiences an effective magnetic field which couples the spin of the electron to its momentum, leading to SO interaction. In heterostrutures, bulk inversion asymmetry (BIA) of the crystal lattice and structural inversion asymmetry (SIA) of the confinement potential give rise to internal electric fields which induce the Dresselhaus [27] and Rashba [28] SO field, respectively. To better understand the SO fields, measurements of their coupling strength have been performed using oscillating electric field [29, 30], Shubnikov-de Haas oscillations [31–33] and antilocalization in magnetoresistance [34, 35].

Here we report anisotropic spin-orbit strength between the crystal axes [110] and [$1\bar{1}0$] of GaAs/AlGaAs heterostructure using ballistic spin resonance (BSR) [8]. An oscillating spin-orbit field is induced by high-frequency bouncing of electrons moving freely in micrometre-scale channels. Electrical measurements of pure spin currents [6] through the channels reveal a suppression in spin relaxation length when the oscillating SO field is in resonance with spin precession in a static field. The observation of different resonance strength in channels oriented along different crystal axis leads to the conclusion of a spin-orbit anisotropy.

5.2 Background

In GaAs 2DEG, the spin-orbit interaction is dominated by first-order couplings to the electron wavevector $\mathbf{k}$. With the coupling constants β (Dresselhaus) and α (Rashba), the effective spin-orbit field can be expressed as

$$\mathbf{B}^{so}(\mathbf{k}) = \frac{2}{g\mu_B}\left[(\alpha - \beta)k_y\hat{x} - (\alpha + \beta)k_x\hat{y}\right] \tag{5.1}$$

where g is the Landé g-factor, μ_B is the Bohr magneton. $\hat{x}$ and $\hat{y}$ define the 2DEG plane and are unit vectors parallel to the [110] and [$\bar{1}$10] crystal axes, respectively.

To create ballistic spin resonance, an oscillating $\mathbf{B}^{so}$ is required. In our experiment, this is achieved by specular scattering of electrons between boundaries of a conducting channel (Fig. 5.1a). An electron following this bouncing trajectory has a periodic momentum $\mathbf{k}$ and experiences therefore an oscillating spin-orbit field. Since the scattering motion is mainly in the transverse direction of the channel, a periodic SO field in the $\hat{x}$ direction (B_x^{so}) is induced in a channel oriented along [110]. Similarly, a periodic B_y^{so} is acting on electrons in a [1$\bar{1}$0] channel. Motion in the longitudinal direction is mostly diffusive, therefore the SO field in the transverse direction is mostly constant unless a small external field (B_z^{ext}) perpendicular to the 2DEG is applied. In this case, electrons are bend into partial cyclotron orbits [8] by the external field and the oscillating motion along $\hat{x}$ and $\hat{y}$ give rise to periodic SO field in both directions (Fig. 5.1b).

In electron spin resonance experiments [36], electron spins are initially polarized along an external magnetic field $\mathbf{B}^{ext}$. If an AC magnetic field is applied perpendicular to the polarization direction at the Larmor frequency of the total field, the spins will oscillate between the up and spin eigenstates of $\mathbf{B}^{ext}$ and a resonance in spin polarization is produced. In ballistic spin resonance, the AC magnetic field is replaced with the periodic SO field described before and the resonance reveals itself as a suppression in spin relaxation length. Since the frequencies of the oscillating SO field and the bouncing motion of electrons are the same, a resonance in spin polarization is expected when the frequency of Larmor precession matches that of a typical bounce:

$$\frac{g\mu_B|\mathbf{B}^{tot}|}{h} \approx \frac{v_F}{2w} \tag{5.2}$$

where h is Planck's constant, w is the width of the channel. v_F is the Fermi velocity and is given by $v_F = \hbar\sqrt{2\pi n_s}/m^*$, with n_s and m^* being the density of the 2DEG and the effective electron mass, respectively. The total field is the sum of the external and SO field: $\mathbf{B}^{tot}(\mathbf{k}) = \mathbf{B}^{ext} + \mathbf{B}^{so}(\mathbf{k})$. When the electrons are following cyclotron orbits that do not cross the entire channel (Fig. 5.1c), in other words when the cyclotron radius is smaller than the channel width $r_c \equiv m^* v_F/eB_z^{ext} < w$, the resonance frequency is replaced by twice the cyclotron frequency $eB_z^{ext}/m\pi$. This modification gives a resonance frequency which changes linearly with an out-of-plane field.

Precession of an electron spin around a changing spin-orbit field causes it to relax, known as the Dyakonov-Perel mechanism [37]. At spin resonance, this relaxation is greatly enhanced as spins are rotated furthest away from their initial polarization direction. The degree of relaxation is mainly determined by the magnitude of the SO field component that is transverse to the initial spin direction. In other words, spin relaxation length measured with an external field pointing in $\hat{y}$ indicates the strength of the oscillating SO field along $\hat{x}$ and vice versa. By comparing BSR strength between a [110] and a [$1\bar{1}0$] channel, one can therefore determine the magnitude of SO coupling and the degree of anisotropy in the system.

5.3 Device and measurements

Two $1\mu m$ wide channels were fabricated on the high mobility GaAs/AlGaAs 2DEG mentioned in Chapter 2; one along the [110] crystal axis and another along [$1\bar{1}0$] (Fig. 5.2). To generate a spin current, electrons are injected into

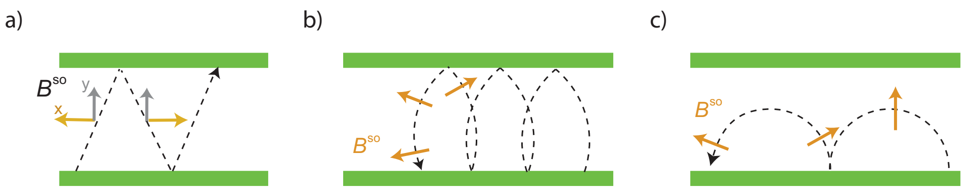

Figure 5.1: Spin-orbit fields induced by periodic motion of ballistic electrons in a narrow channel. a) Electrons bounce between channel boundaries and induce an oscillating spin-orbit field in the longitudinal direction of the channel. b) At the presence of a weak out-of-plane field, motion of electrons is composed of bouncing and partial cyclotron orbits and a small transverse component is added to the oscillating SO field. c) At a stronger out-of-plane field, electrons only follow skipping orbits smaller than the width of the channel and the SO field is periodic in both directions. Figure adapted from [8].

the channels through spin-selective QPCs at a temperature of 600mK. By tuning the QPCs to the first conductance plateau (e^2/h) at the presence of an in-plane field $\mathbf{B}^{ext}$, only electrons with a spin parallel to the field direction are transmitted [6, 38]. The injected charges are drained at the left end of the channels, while spin polarization accumulated above the injectors diffuses to both ends of the channels, generating a pure spin current to the right of the injectors. With a Fermi velocity of $1.1 \times 10^5 m/s$, the bouncing frequency is about 70 GHz. Due to the long mean free path of $\sim 20\mu m$, this frequency is maintained for several bounces before the momentum of the electrons is randomized by scatterings.

Polarization of the spin current can be measured by the non-local voltage, V_{nl}, that develops across the spin-selective detector QPCs located $25\mu m$ to the right of the injectors. The non-local voltage measures the difference in chemical potential between spins above the detector and those at the right drain where the polarization is zero. This non-local spin signal increases monotonically with spin relaxation length λ_s [6]:

$$V_{nl}(\lambda_s) = K(\lambda_s)\frac{\rho_\square}{w} I_{inj} P_{inj} P_{det} \tag{5.3}$$

where

$$K(x) = \frac{x \sinh(\frac{L_r - x_{id}}{x})}{\sinh(L_r/x)\,[\coth(L_r/x) + \coth(L_l/x)]}, \tag{5.4}$$

$\rho_\square$ is the sheet resistance, I_{inj} the injected current, $P_{inj(det)}$ the injector(detector) polarization, x_{id} the distance from injector to detector and $L_{l(r)}$ the distance between injector and left(right) end of the channels. For this experiment, $L_l = 50\mu m$ and $L_r = 80\mu m$.

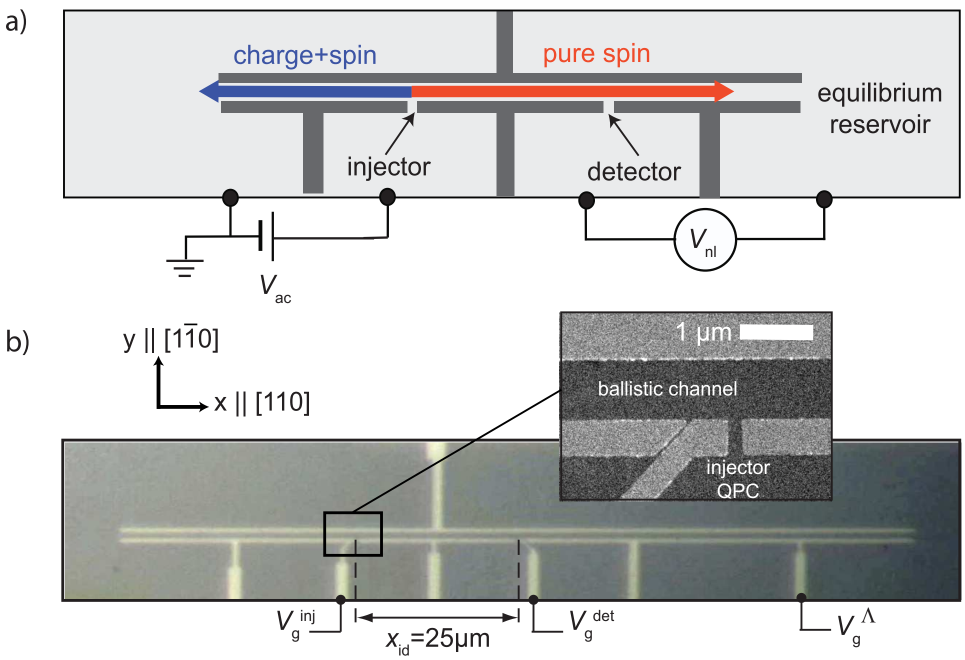

Figure 5.2: a) Simplified diagram of a pure spin current measurement. Gates (dark grey) deplete the 2DEG to define the injector and detector QPCs and the ballistic channel. b) Optical image of a [110] channel with CrAu gates in light grey. Gate voltages V_g^{inj} and V_g^{det} tune QPCs to the spin-polarized plateaus. Undepleting the Λ-gate (V_g^{Λ}) changes the distance from the injector to the right reservoir from $L_r = 80\mu m$ to $L_{r-short} = 50\mu m$. The width of the channel is $1\mu m$. Inset: SEM of the injector area. Figure and caption are adapted from [8].

5.4 Results and discussions

The non-local voltage, measured at high magnetic field with the [110] channel, shows the capability of QPCs to inject and detect spin current. Fig: 5.3 shows injector and detector scans of the non-local voltage. When both QPCs are tuned to the first conductance plateau, a positive non-local voltage can be seen at the lower left corner of the scans indicating a spin population above the detector. At the third conductance plateau, two spin-up and one spin-down channel is transmitted. This gives a smaller spin polarization and so the smaller positive voltages at the other three corners of the scans. The voltage vanishes however, when only one QPC is spin polarized or neither of them is. Since the spin polarization is expected to increase monotonically with field [6], the drop in spin signal from 2T (Fig. 5.3a) to 4T (Fig. 5.3b) and the jump back up at 8T (Fig. 5.3c) are the signs of a spin resonance at 4T.

To determine the degree of anisotropy in the 2DEG, we tune both injector and detector to their first polarized plateau and measure the non-local signal at different external field $\mathbf{B}^{ext}$. At zero out-of-plane field B_z^{ext}, the absence of an oscillating SO field in the transverse direction of the channel implies no resonance when $\mathbf{B}^{ext}$ is applied in-plane and parallel to the channel. This can be seen in Fig. 5.4a, b: the non-local spin signals increase steadily with the parallel field as a result of increasing QPC polarization. But when the in-plane field is applied perpendicular to the channel orientation, we observe a big contrast in the resonance strength between [110] and [$1\bar{1}0$]. In [110] channel, the non-local signal has completely collapsed at $B_y^{ext} \sim 5T$, which indicates that the spins have all relaxed before reaching the detector. This observation is a close match to the strong BSR reported in earlier experiments on the same channel orientation [8]. Same non-local measurement performed on the [$1\bar{1}0$] channel showed, however, quite different BSR feature: the resonance dip does not cause a breakdown in V_{nl} but is instead much shallower and occurs at a higher field. Since the strength of resonance in [110] depends primarily on $B_x^{so} \propto (\alpha - \beta)k_F$ and mainly on $B_y^{so} \propto (\alpha + \beta)k_F$ for [$1\bar{1}0$], we can qualitatively conclude a stronger SO coupling in $\hat{x}$ direction and therefore a spin-orbit anisotropy. The discrepancy in resonance frequency is not very crucial to estimating the degree of relaxation and can be explained by a narrower $[1\bar{1}0]$ channel or different electron density which usually varies with device and cooldown (to change the external field direction).

To further support our argument of an anisotropic SO field, we measure BSR due to an oscillating SO field in the transverse direction introduced by a small B_z^{ext}. Spin signals at an external field parallel to the channels reveal quite different resonance features, again. The observed BSRs in [110] are weak but become stronger with increasing B_z^{ext}. While in $[1\bar{1}0]$, the BSR strength grows faster with B_z^{ext} and by $B_z^{ext} = 70mT$ the non-local signal has dropped to near zero as in B_y^{ext} measurement of [110] channel. The growing strength and movement in B_x^{ext} of the BSRs are explained by the faster oscillating SO field at higher cyclotron frequency. As the resonance strength of the $[1\bar{1}0]$ ([110]) channel depends on SO field in $\hat{x}$ ($\hat{y}$) direction, a similar BSR is expected in both channels if the SO field is isotropic. The zero spin resonance signal in the $[1\bar{1}0]$ channel is, therefore, another evidence of a stronger SO field in $\hat{x}$ direction. The less dramatic shift in B_y^{ext} of the BSR dip in $[1\bar{1}0]$ also reinforces our hypothesis that the channel is narrower: the resonance frequency (and therefore B_y^{ext}) does not change until the cyclotron radius falls below the channel width which happens at about $B_z^{ext} \approx 40mT$ for a $1\mu m$ wide channel. This change can easily be seen in the [110] channel but for $[1\bar{1}0]$ there is no significant change until $B_z^{ext} \approx 47mT$ which implies a shorter width of $\sim 0.8\mu m$ for the $[1\bar{1}0]$ channel.

To get a better sense on the degree of spin relaxation and to find a rough estimation on the magnitude of anisotropy, we calculate the spin relaxation length from the ratio of non-local signal at BSR and the nonresonance spin signal V_{nl}^0 of the corresponding channel (B_x^{ext} trace for [110] channel and B_y^{ext} for $[1\bar{1}0]$). By assuming that the injector and detector polarization in spin resonance are the same as without resonance, the ratio is only dependent on the spin relaxation length: $\frac{V_{nl}}{V_{nl}^0} = \frac{K(\lambda_s)}{K(\lambda_s^0)}$ where λ_s^0 is the nonresonance relaxation length associated with V_{nl}^0. By undepleting the Λ-gate and shortening the right end of the channel to $L_{r-short} = 50\mu m$, one can use the non-local spin signal for the shorter channel to extract λ_s^0 [6, 8]. The calculated spin relaxation length from the ratio shows the different magnitude of spin relaxation caused by SO interaction (Fig. 5.6). For clarity of comparison, the spin relaxation lengths have been normalized with λ_s^0 due to the quite different nonresonance λ_s^0 between the channels (about $10\mu m$). At resonance, the spin-orbit field B_x^{so} causes spins oriented along $\hat{y}$ to relax at least 40% faster, while B_y^{so} only reduces the relaxation length of $\hat{x}$-oriented spins by about 25%. This demonstrates a decent anisotropy in the spin-orbit field. If the same mean free path is assumed for different channels and cooldowns, the anisotropy ratio is [39]: $(\alpha-\beta)/(\alpha+\beta) = \sqrt{\lambda_{s,\hat{x}}/\lambda_{s,\hat{y}}} \sim 1.2-1.7$, where $\lambda_{s,\hat{x}}$ and $\lambda_{s,\hat{y}}$ are the spin relaxation length at resonance of spins aligned along $\hat{x}$ and $\hat{y}$, respectively. A comparison with Monte Carlo simulation on spin relaxation length that accounts for different mean free path and channel width will be needed to obtain a more accurate read on the magnitude of anisotropy.

In conclusion, we observed spin-orbit field anisotropy in GaAs/AlGaAs 2DEG by measuring the spin relaxation length of differently oriented spins with ballistic spin resonance. An initial estimation from the relaxation lengths puts the anisotropy ratio at about 1.2 to 1.7.

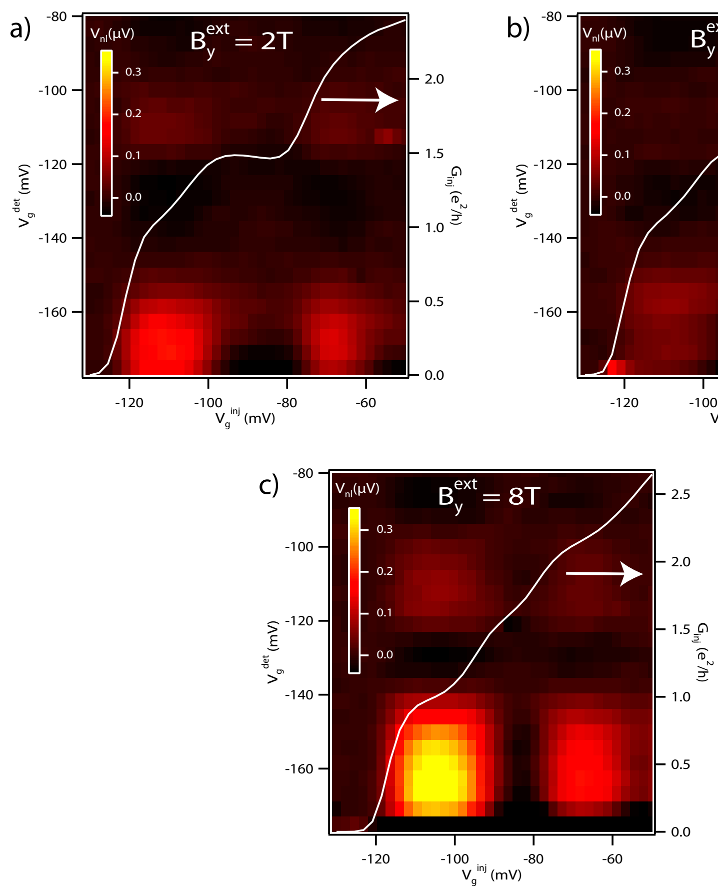

Figure 5.3: Injector and detector scans of non-local voltage V_{nl} at high magnetic field. [110] channel is used and the external magnetic field is along $\hat{y}$. Conductance of the injector QPC (G_{inj}) is also shown (white curve). a) Non-local signal at a field below resonance. V_{nl} is non-zero only when both injector and detector are tuned to polarized conductance plateaus (odd number plateaus). b) V_{nl} measured at resonance. The spin signal has dropped significantly to near zero. c) V_{nl} at a field above resonance. At higher field, QPCs are more polarized and a stronger spin signal is observed.

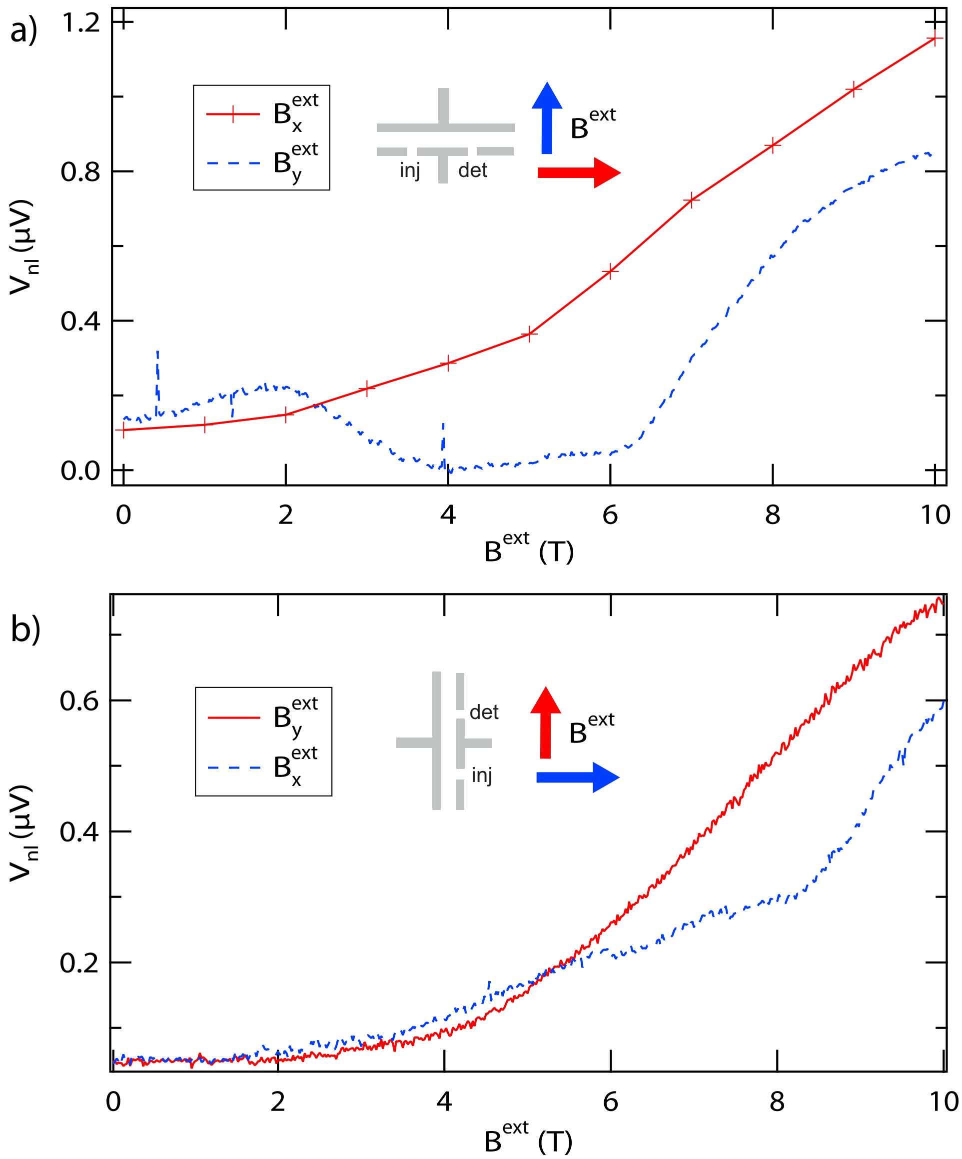

Figure 5.4: Ballistic spin resonance due an oscillating spin-orbit field. The resonance (blue curves) observed in a channel oriented along [110] (a) and [1$\bar{1}$0] (b) is due to an oscillating SO field along $\hat{x}$ and $\hat{y}$, respectively. When the external field is parallel to the channel, no BSR is observed (red curves). The different magnitude of the BSR dips indicates an anisotropy in the SO field.

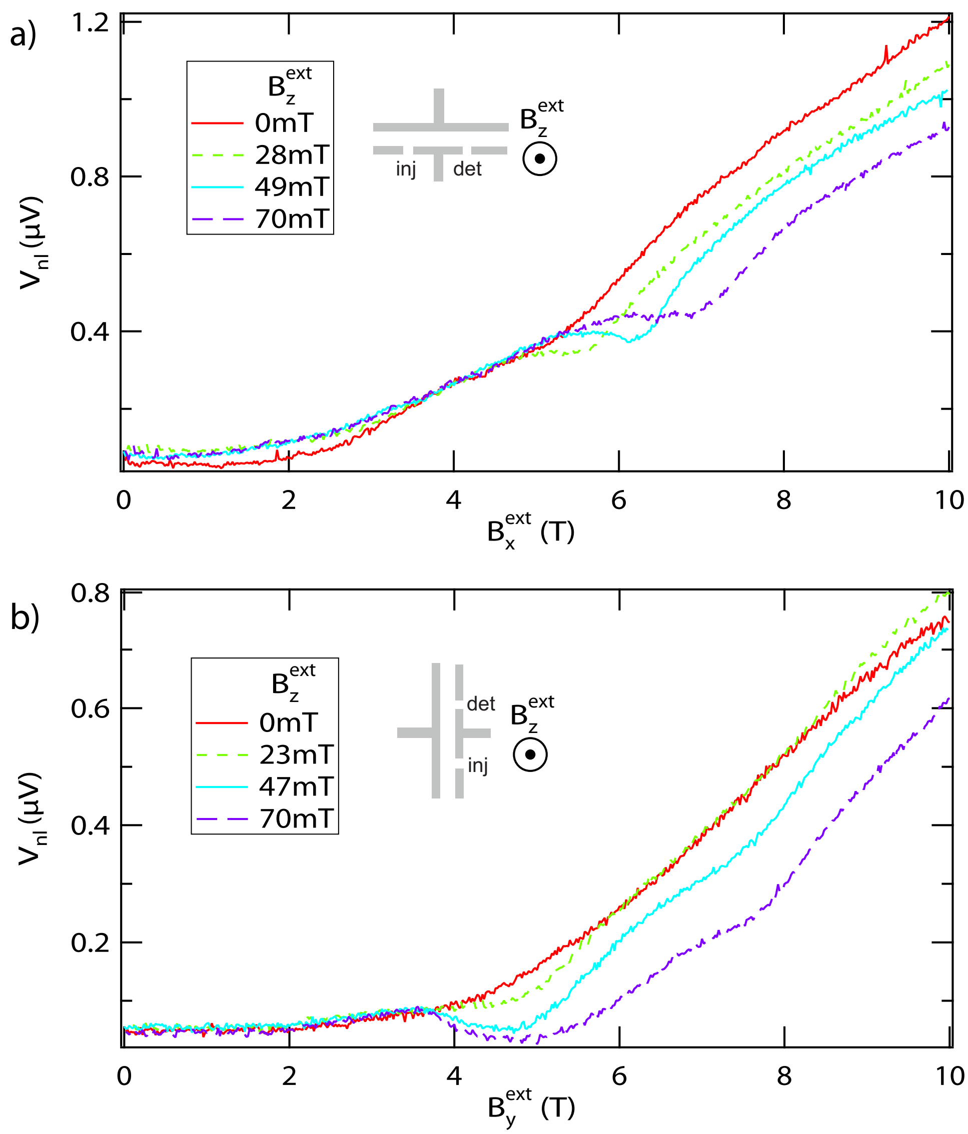

Figure 5.5: When the field is parallel to the channel, BSR can be induced by applying an out-of-plane field B_z^{ext}. Strength of the spin resonance in a channel along [110] (a) and [1$\bar{1}$0] (b) is a measure of the spin-orbit field along $\hat{y}$ and $\hat{x}$, respectively. The contrast in magnitude of BSR implies anisotropy in the spin-orbit field.

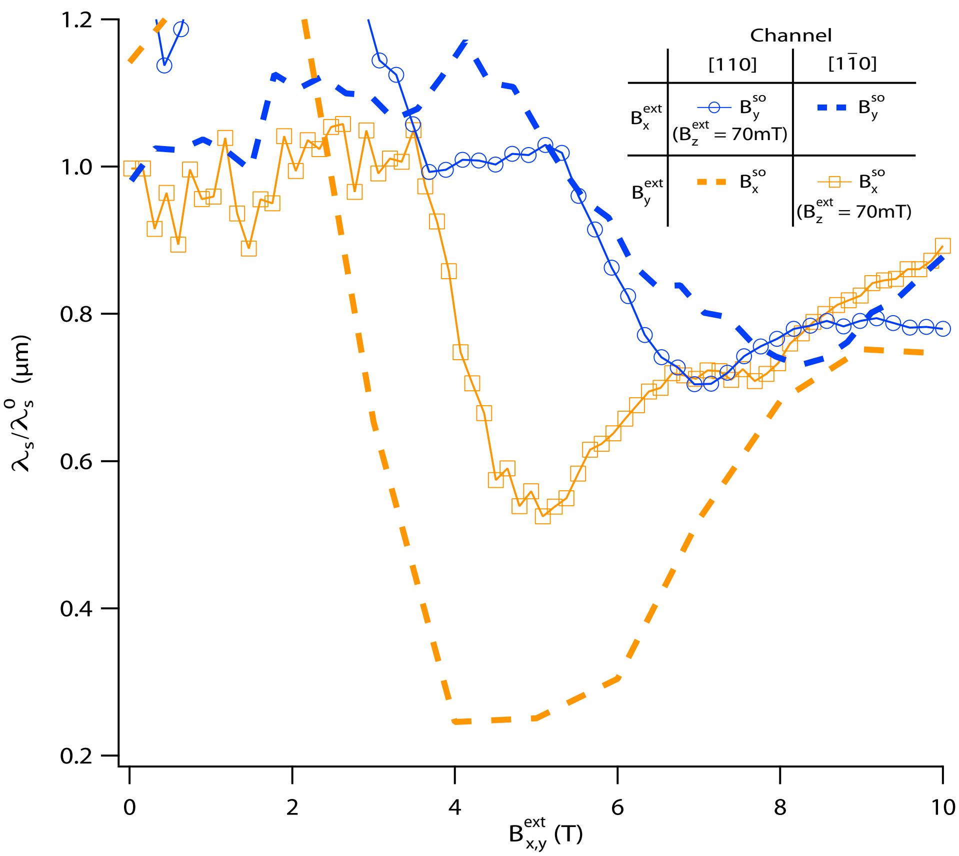

Figure 5.6: Spin relaxation length at resonance λ_s normalized by the non-resonance spin relaxation length λ_s^0. A large reduction in λ_s is observed when $\hat{y}$-oriented spins are relaxed by a SO field along $\hat{x}$ (orange curves). λ_s is reduced by a smaller amount when $\hat{x}$-oriented spins experiences a SO field along $\hat{y}$ (blue curves). The inset table shows the external field and channel orientation of the measured BSR and the component of $\mathbf{B}^{so}$ responsible for the resonance.

Bibliography

[1] M. N. Baibich, J. M. Broto, A. Fert, F. Nguyen Van Dau, F. Petroff, P. Etienne, G. Creuzet, A. Friederich, and J. Chazelas. Giant Magnetoresistance of (001)Fe/(001)Cr Magnetic Superlattices. *Phys. Rev. Lett.*, 61:2472–2475, 1988.

[2] G. Binasch, P. Grünberg, F. Saurenbach, and W. Zinn. Enhanced magnetoresistance in layered magnetic structures with antiferromagnetic interlayer exchange. *Phys. Rev. B*, 39:4828–4830, 1989.

[3] Gary A. Prinz. Magnetoelectronics. *Science*, 282:1660–1663, 1998.

[4] S. Yuasa, T. Nagahama, A. Fukushima, Y. Suzuki, and K. Ando. Giant room-temperature magnetoresistance in single-crystal Fe/MgO/Fe magnetic tunnel junctions. *Nature Materials*, 3:868–871, 2004.

[5] S. S. P. Parkin, C. Kaiser, A. Panchula, P. M. Rice, B. Hughes, M. Samant, and S.-H. Yang. Giant tunnelling magnetoresistance at room temperature with MgO (100) tunnel barriers. *Nature Materials*, 3:862–867, 2004.

[6] S. M. Frolov, A. Venkatesan, W. Yu, J. A. Folk, and W. Wegscheider. Electrical Generation of Pure Spin Currents in a Two-Dimensional Electron Gas. *Phys. Rev. Lett.*, 102:116802, 2009.

[7] C. W. J. Beenakker and H. van Houten. Quantum Transport in Semiconductor Nanostructures. *Solid State Phys.*, 4, 1991.

[8] S. M. Frolov, S. Lüscher, W. Yu, Y. Ren, J. A. Folk, and W. Wegscheider. Ballistic spin resonance. *Nature*, 458:868–871, 2009.

[9] B. J. van Wees, L. P. Kouwenhoven, H. van Houten, C. W. J. Beenakker, J. E. Mooij, C. T. Foxon, and J. J. Harris. Quantized conductance of magnetoelectric subbands in ballistic point contacts. *Phys. Rev. B*, 38:3625–3627, 1988.

[10] S. Datta. *Electronic Transport in Mesoscopic Systems*. Cambridge University Press, 1995.

[11] L. P. Kouwenhoven, C. M. Marcus, P. L. McEuen, S. Tarucha, R. M. Westervelt, and Wingreen N. S. Electron Transport in Quantum Dots. In L. L. Sohn and et al., editors, *Mesoscopic Electron Transport*. Kluwer, 1997.

[12] N. Craig and T. Lester. Hitchhiker's Guide to the Dilution Refrigerator. `http://marcuslab.harvard.edu/how_to/Fridge.pdf`, 2004.

[13] M. Field, C. G. Smith, M. Pepper, D. A. Ritchie, J. E. F. Frost, G. A. C. Jones, and D. G. Hasko. Measurement of Coulomb blockade with a noninvasive voltage probe. *Phys. Rev. Lett.*, 70:1311–4, 1993.

[14] D. Sprinzak, Yang Ji, M. Heiblum, D. Mahalu, and Hadas S. Charge Distribution in a Kondo-Correlated Quantum Dot. *Phys. Rev. Lett.*, 88:176805, 2002.

[15] R. Hanson, L. H. Willems van Beveren, I. T. Vink, J. M. Elzerman, W. J. M. Naber, F. H. L. Koppens, L. P. Kouwenhoven, and L. M. K. Vandersypen. Single-Shot Readout of Electron Spin States in a Quantum Dot Using Spin-Dependent Tunnel Rates. *Phys. Rev. Lett.*, 94:196802, 2005.

[16] J. M. Elzerman, R. Hanson, J. S. Greidanus, L. H. Willems van Beveren, S. De Franceschi, L. M. K. Vandersypen, S. Tarucha, and L. P. Kouwenhoven. Few-electron quantum dot circuit with integrated charge read out. *Phys. Rev. B*, 67:161308, 2003.

[17] L. DiCarlo, H. J. Lynch, A. C. Johnson, L. I. Childress, K. Crockett, C. M. Marcus, M. P. Hanson, and A. C. Gossard. Differential Charge

Sensing and Charge Delocalization in a Tunable Double Quantum Dot. *Phys. Rev. Lett.*, 92:226801, 2004.

[18] J. R. Petta, A. C. Johnson, J. M. Taylor, E. A. Laird, A. Yacoby, M. D. Lukin, C. M. Marcus, M. P. Hanson, and A. C. Gossard. Coherent Manipulation of Coupled Electron Spins in Semiconductor Quantum Dots. *Science*, 309:2180–2184, 2005.

[19] A. C. Johnson, C. M. Marcus, M. P. Hanson, and A. C. Gossard. Coulomb-Modified Fano Resonance in a One-Lead Quantum Dot. *Phys. Rev. Lett.*, 93:106803, 2004.

[20] M. Sato, H. Aikawa, K. Kobayashi, S. Katsumoto, and Y. Iye. Observation of the Fano-Kondo Antiresonance in a Quantum Wire with a Side-Coupled Quantum Dot. *Phys. Rev. Lett.*, 95:066801, 2005.

[21] T. Otsuka, E. Abe, S. Katsumoto, Y. Iye, G. L. Khym, and Kang K. Fano Effect in a Few-Electron Quantum Dot. *Journal of the Phys. Soc. of Japan*, 76:084706, 2007.

[22] U. Fano. Effects of Configuration Interaction on Intensities and Phase Shifts. *Phys. Rev.*, 124:1866–1878, 1961.

[23] J. Göres, D. Goldhaber-Gordon, S. Heemeyer, M. A. Kastner, Hadas Shtrikman, D. Mahalu, and U. Meirav. Fano resonances in electronic transport through a single-electron transistor. *Phys. Rev. B*, 62:2188–2194, 2000.

[24] A. G. Aronov and Y. B. Lyanda-Geller. Spin-orbit Berry phase in conducting rings. *Phys. Rev. Lett.*, 70:343–346, 1993.

[25] T. Koga, J. Nitta, H. Takayanagi, and S. Datta. Spin-Filter Device Based on the Rashba Effect Using a Nonmagnetic Resonant Tunneling Diode. *Phys. Rev. Lett.*, 88:126601, 2002.

[26] A. A. Kiselev and K. W. Kim. T-shaped ballistic spin filter. *Appl. Phys. Lett.*, 78:775–777, 2001.

[27] G. Dresselhaus. Spin-Orbit Coupling Effects in Zinc Blende Structures. *Phys. Rev.*, 100:580–586, 1955.

[28] E. I. Rashba. Properties of semiconductors with an extremum loop. *Sov. Phys. Solid State*, 2:1224–1238, 1960.

[29] L. Meier, G. Salis, I. Shorubalko, E. Gini, S. Schon, and K. Ensslin. Measurement of Rashba and Dresselhaus spin-orbit magnetic fields. *Nature Phys.*, 3:650–654, 2007.

[30] K. C. Nowack, F. H. L. Koppens, Yu. V. Nazarov, and L. M. K. Vandersypen. Coherent Control of a Single Electron Spin with Electric Fields. *Science*, 318:1430–1433, 2007.

[31] J. Luo, H. Munekata, F. F. Fang, and P. J. Stiles. Effects of inversion asymmetry on electron energy band structures in GaSb/InAs/GaSb quantum wells. *Phys. Rev. B*, 41:7685–7693, 1990.

[32] G. Engels, J. Lange, Th. Schäpers, and H. Lüth. Experimental and theoretical approach to spin splitting in modulation-doped $In_xGa_{1-x}As$/InP quantum wells for B→0 . *Phys. Rev. B*, 55:R1958–R1961, 1997.

[33] Th. Schäpers, G. Engels, J. Lange, Th. Klocke, M. Hollfelder, and H. Lüth. Effect of the heterointerface on the spin splitting in modulation doped $In_xGa_{1-x}As$/InP quantum wells for B→0. *Journal of Appl. Phys.*, 83:4324–4333, 1998.

[34] T. Koga, J. Nitta, T. Akazaki, and H. Takayanagi. Rashba Spin-Orbit Coupling Probed by the Weak Antilocalization Analysis in InAlAs/InGaAs/InAlAs Quantum Wells as a Function of Quantum Well Asymmetry. *Phys. Rev. Lett.*, 89:046801, 2002.

[35] J. B. Miller, D. M. Zumbühl, C. M. Marcus, Y. B. Lyanda-Geller, D. Goldhaber-Gordon, K. Campman, and A. C. Gossard. Gate-Controlled Spin-Orbit Quantum Interference Effects in Lateral Transport. *Phys. Rev. Lett.*, 90:076807, 2003.

[36] Y. K. Zavoisky. Spinmagnetic resonance in paramagnetics. *J. Phys. USSR*, 9:245–246, 1945.

[37] M. I. Dyakonov and V. I. Perel. Spin relaxation of conduction electrons in noncentrosymmetric semiconductors. *Sov. Phys. Solid State*, 13, 1972.

[38] R. M. Potok, J. A. Folk, C. M. Marcus, and V. Umansky. Detecting Spin-Polarized Currents in Ballistic Nanostructures. *Phys. Rev. Lett.*, 89:266602, 2002.

[39] N. S. Averkiev and L. E. Golub. Giant spin relaxation anisotropy in zinc-blende heterostructures. *Phys. Rev. B*, 60:15582–15584, 1999.

Appendix A

Device fabrication

The following are the step by step details of device fabrication processes used for the experiments.

A.1 Cleaning and dicing

- Heterostructure wafer is cleaved into suitable sizes (about 5mm $\times$ 4mm) using a carbide scriber.

- Ultrasound cleaning in 3-solvents for 5 minutes each. First in TCE (Trichloroethylene), then acetone and methanol. Chip is blow-dried and hotplate baked at 120°C for 5 minutes to remove solvent residues.

A.2 Photolithography for ohmics

- Shipley 1813 photoresist is spun at 5000rpm for 45 seconds. Then hotplate baked at 120°C for 2mins. This gives a thickness of about $1\mu m$ away from the edges. (Optional step: Soak in toluene for 5mins to harden the surface of the resist to create undercut for easier liftoff).

- Ohmics pattern is aligned and exposed for 90secs using Karl Suss MJB-3 75mm mask aligner. Optimal exposure time is determined by running multiple tests on dummy chips. The mask is made of iron oxide on glass plate and the pattern is designed by Sergey Frolov.

- The exposed photoresist is developed in Microposit MF CD-26 for 1min, then rinsed in DI water for another 1min. Chip is checked under microscope with UV filter on to confirm quality of the developed patterns. Additional pattern (usually used for patching purposes) can be exposed by shining a spot of unfiltered light with a microscope set to highest power and magnification. This method was discovered by George Kamps.

- Chip is oxygen plasma cleaned for 25secs in a PECVD, then dipped into Ammonium Hydroxide and blow-dried.

A.3 Deposition, annealing and testing of ohmics

- Ohmic metals are thermally evaporated following the recipe:

  1. 50Å Ni (bottom layer)
  2. 400Å Ge
  3. 800Å Au
  4. 250Å Ni
  5. 750Å Au

  Each layer is evaporated at about 2Å/s.

- Liftoff in 90°C hot acetone in a beaker sealed with Parafilm to avoid acetone drying out. Chip is placed in a Petri dish covered by acetone and checked under microscope to ensure liftoff is successful. Methanol is then used to remove the acetone.

- The ohmic metals are thermally annealed at 410°C for 3mins in a chamber filled with forming gas (about 6% H_2 balance N_2) at 100mmHg. Annealing time can change depending on the depth of the 2DEG. 3mins was found to be optimal for the 110nm deep D041008B heterostructure.

- Chip is glued on a non-magnetic 32 pins chip carrier with PMMA. To test the ohmics, they are wire-bonded and dipped into liquid helium. The typical resistance for good ohmic contacts are less than a few $k\Omega$. If most of the ohmics have much higher resistance, another fabrication run of ohmics on a different chip will be needed. If the ohmics are reliable, the chip can be used for patterning of smaller gate and lead structures.

A.4 Etching of mesas

- Before putting gate structures, a wet etching step is performed to define area of mesas and to remove the 2DEG around some of the ohmic pads, so that they can be used as bondpads for gates. Mask for the etching is made using electron beam (e-beam) lithography.
- Chip is first 3-solvent cleaned and baked. Then a layer 950K C3 PMMA (3% of 950K molecular weight PMMA dissolved in chlorobenzene) e-beam resist is spun at 3500rpm for 40s and baked at 180°C for 10mins. This will give a thickness of about 250nm.
- All patterns for e-beam lithography are designed in LASI 7 and written using a Raith e-beam system at 4Dlabs of Simon Fraser University. For wet etching, patterns are written at 10keV, 60μm aperture, 200nm area step size, and 150$\mu C/cm^2$. These exposure parameters vary with each e-beam system, and should be optimized by running exposure matrices on dummy chips. Since exposure dose changes with reflectivity of sample surface, the dummy chips should have the same surface layer as that of the heterostructure.
- Exposed patterns are developed in a 1:3 solution of methyl isobutyl ketone (MIBK):isopropanol (IPA) for 90secs. Then it's dipped into IPA for 30secs and blow-dried.
- Etching is done in a solution of 1:8:240 of H_2SO_4:H_2O_2:H_2O. Before the heterostructure is etched, a GaAs dummy chip is used to determine the etch rate. The dummy chip is dipped into the acid mixture for a minute and profiled with an Alpha-step profilometer. Typical etch rate is about 1-2nm/s. Then, the heterostructure is etched to the depth of the 2DEG and rinsed with DI water.

A.5 Fabrication of gate structures

- The next step is to put finer gate and lead structures onto the heterostructure surface. This involves writing two e-beam lithographical patterns: fine gate structures (smaller than a few microns in size) and leads that connect them to the gate bondpads.

- For fine gates, the chip is cleaned and baked, then a $80nm$ layer of A2 950K PMMA (dissolved 2% in anisol) is spun at 3500rpm for 40s and baked at 180°C for 10mins. Gate patterns are written in $30keV$, $10\mu m$ aperture and $12nm$ step size. Optimal dose for fine gates ranges from $150 - 300\mu C/cm^2$. After the patterns have been developed like in the etch step, gate metals are deposited in a thermal evaporator. A deposition of 30Å Cr and 90Å Au has worked well for the experiments. To liftoff, the chip is usually soaked in hot acetone for at least an hour and ultrasound for a few seconds. Avoid applying excessive ultrasound, as it may rip the fine metals off the surface. In parallel with writing on the heterostructure, the same patterns should be written on a dummy chip using the same exposure parameters and same gate metals should be evaporated. This dummy chip is imaged with e-beam microscope to check the quality of the patterns before evaporating the heterostructure. This avoids exposing electron beams directly to a heterostructure which can cause damage to the 2DEG.

- To make leads that connect the fine gates to the gate bondpads, a bilayer of C8 250K ($450nm$) and C3 950K ($250nm$) PMMA is used. Each layer is spun at 3500rpm for 40s and baked at 180°C for 5min. The lower molecular weight of the bottom layer causes an undercut which facilitates liftoff. The leads, which are usually about $5\mu m$ wide, are written in $10keV$, $60\mu m$ aperture, $200nm$ step size and around $250\mu C/cm^2$.

- Finally, the chip is glued and wire-bonded to a chip carrier and ready to be cooled to low temperature for data gathering.